Title

Transplantation of wild-type mouse hematopoietic stem and progenitor cells ameliorates deficits in a mouse model of Friedreichs ataxia.

Permalink

https://escholarship.org/uc/item/7tb3137c

Journal

Science Translational Medicine, 9(413)

Authors

Rocca, Celine
Goodman, Spencer
Dulin, Jennifer
et al.

Publication Date

2017-10-25

DOI

10.1126/scitranslmed.aaj2347

Peer reviewed

Transplantation of wild-type mouse hematopoietic stem and progenitor cells ameliorates deficits in a mouse model of Friedreich's ataxia

Celine J. Rocca[1], **Spencer M. Goodman**[1], **Jennifer N. Dulin**[2], **Joseph H. Haquang**[1], **Ilya Gertsman**[1], **Jordan Blondelle**[3], **Janell L. M. Smith**[1], **Charles J. Heyser**[2], and **Stephanie Cherqui**[1,*]

[1]Division of Genetics, Department of Pediatrics, University of California, San Diego, La Jolla, CA 92093, USA

[2]Department of Neurosciences, University of California, San Diego, La Jolla, CA 92093, USA

[3]Division of Cardiovascular Medicine, University of California, San Diego, La Jolla, CA 92093, USA

Abstract

Friedreich's ataxia (FRDA) is an incurable autosomal recessive neurodegenerative disease caused by reduced expression of the mitochondrial protein frataxin due to an intronic GAA-repeat expansion in the *FXN* gene. We report the therapeutic efficacy of transplanting wild-type mouse hematopoietic stem and progenitor cells (HSPCs) into the YG8R mouse model of FRDA. In the HSPC-transplanted YG8R mice, development of muscle weakness and locomotor deficits was abrogated as was degeneration of large sensory neurons in the dorsal root ganglia (DRGs) and mitochondrial capacity was improved in brain, skeletal muscle, and heart. Transplanted HSPCs engrafted and then differentiated into microglia in the brain and spinal cord and into macrophages in the DRGs, heart, and muscle of YG8R FRDA mice. We observed the transfer of wild-type frataxin and Cox8 mitochondrial proteins from HSPC-derived microglia/macrophages to FRDA mouse neurons and muscle myocytes in vivo. Our results show the HSPC-mediated phenotypic rescue of FRDA in YG8R mice and suggest that this approach should be investigated further as a strategy for treating FRDA.

INTRODUCTION

Friedreich's ataxia (FRDA) is a multisystemic autosomal recessive disease predominantly caused by GAA-repeat hyperexpansion within the first intron of the frataxin gene (*FXN*) (1). Long GAA repeats cause reduced expression of frataxin, a highly conserved mitochondrial protein mainly expressed in mitochondria-rich tissues including the nervous system, muscle, and heart (2). Although its function is not fully elucidated, frataxin is known to be an iron-binding protein participating in Fe-S cluster assembly. In the absence of frataxin, iron accumulates within mitochondria, leading to defective iron-mediated biosynthetic processes and increased oxidative stress (3–5). Pathologically, frataxin insufficiency leads to spinocerebellar neurodegeneration, ataxia, muscle weakness, and cardiomyopathy (1, 6). The primary pathological cause of the neuropathy is the loss of large sensory neurons in the dorsal root ganglia (DRGs), particularly in the lumbar region (7, 8), and the atrophy of dentate nuclei in the cerebellum (9). The transgenic YG8R mouse model, which exclusively expresses two mutant human *FXN* transgenes (h*FXN*) containing GAA expansions, develops progressive neurological degeneration with locomotor and coordination deficits and muscle weakness (10). Among transgenic FRDA mouse models expressing human *FXN* with expanded repeats, YG8R is the most severe model exhibiting substantial coordination and locomotor deficits by 3 months of age (11, 12).

Human hematopoietic stem and progenitor cells (HSPCs) from the bone marrow are ideal candidates for use in regenerative medicine and cell replacement therapy because of their ease of isolation, self-renewal capacity, and safety. Although the ability of HSPC transplantation to rescue nonhematopoietic tissue remains contentious, we previously demonstrated that a single systemic transplant of wild-type mouse HSPCs led to long-term kidney, eye, and thyroid preservation in a mouse model of the multisystemic lysosomal storage disorder cystinosis (13–16). In this mouse model, the disease phenotype was rescued by the differentiation of wild-type HSPCs into macrophages that delivered lysosomes bearing functional cystinosin into diseased host cells potentially through long tubular extensions known as tunneling nanotubes (17). Tunneling nanotubes have been described as an intercellular delivery route for chemical mediators, proteins, and organelles such as lysosomes and mitochondria (18–20). We hypothesized that transplantation of wild-type mouse HSPCs could provide a delivery vehicle for functional fra-taxin and thereby alleviate disease progression in a mouse model of FRDA in which the mice express the mutant human frataxin (*FXN*) gene. Here, we report that wild-type mouse HSPC transplantation into young YG8R mice rescued many aspects of the FRDA phenotype including coordination and locomotion deficits and vacuolar degeneration of DRG neurons.

RESULTS

Transplantation of wild-type mouse HSPCs prevents the onset of severe locomotor deficits in YG8R mice

To investigate the potential of wild-type mouse HSPC transplantation for treating FRDA, we intravenously injected lethally irradiated 2-month-old YG8R (mfxn$^{-/-}$ hFXN$^+$) mice with wild-type green fluorescent protein (GFP)–expressing or DsRed-expressing Sca1$^+$ mouse HSPCs ($n = 13$). Donor-derived HSPC engraftment ranged from 35 to 96% (expressed as a

percentage of GFP-positive white blood cells in peripheral blood) (table S1). As controls, we analyzed wild-type YG8R littermates ($n = 16$), nontransplanted YG8R littermates ($n = 4$), or lethally irradiated YG8R mice transplanted with YG8R (mfxn$^{-/-}$ hFXN$^+$) HSPCs ($n = 5$). YG8R mice exhibited a progressive decrease in locomotor activity and coordination deficits by 3 months of age (10, 12). Thus, we assessed sensory function, motor function, and muscle strength for each group at both 5 and 9 months of age (3 and 7 months after transplantation, respectively). No difference in performance was observed in any of the behavioral tests at either time point between nontransplanted YG8R mice and those transplanted with mfxn$^{-/-}$ hFXN$^+$ (control) HSPCs (Fig. 1A), indicating that neither irradiation nor transplantation with mfxn$^{-/-}$ hFXN$^+$ HSPCs ameliorated the disease phenotype. Compared to wild-type mice, YG8R mice and those transplanted with mfxn$^{-/-}$hFXN$^+$ (control) HSPCs displayed reduced open-field locomotor activity, impaired coordination in the rotarod test, and alterations in gait, as well as decreased forelimb grip strength at both time points (Fig. 1A), consistent with previous reports (10, 12). In contrast, YG8R mice transplanted with wild-type mouse HSPCs exhibited normal locomotor activity and muscle strength at both 3 and 7 months after transplantation (Fig. 1A). Together, these data demonstrated that wild-type mouse HSPC transplantation in 2-month-old YG8R mice rescued the progressive neurobehavioral and muscular deficits characteristic of this FRDA animal model. In contrast to our previous findings in a cystinosis model (14, 16), the YG8R mouse exhibiting the lowest percentage of donor-derived cell engraftment (35%; table S1) still exhibited physiological rescue of the behavioral deficits (table S2).

Wild-type mouse HSPC transplantation prevents the degeneration of large sensory neurons in YG8R mice

Neuropathology in FRDA results, in part, from degeneration of large sensory neurons in DRGs (8), causing the formation of large vacuoles within the lumbar DRGs of YG8R mice (10). Vacuolar accumulation in lumbar level 5 (L5) DRG neurons was detected in 9-month-old YG8R control mice with no significant difference in vacuolar area between nontransplanted and mfxn$^{-/-}$ hFXN$^+$ HSPC-transplanted YG8R mice ($P = 0.5408$; Fig. 1B). In contrast, YG8R mice transplanted with wild-type mouse HSPCs exhibited a significant reduction in vacuolar area that was comparable to that of wild-type mice ($P < 0.005$; Fig. 1B).

Wild-type mouse HSPCs differentiate into phagocytic cells after engraftment in the mouse nervous system

Given that FRDA affects the central nervous system (CNS) in addition to peripheral sensory neurons (8), we next investigated the engraftment and differentiation of wild-type mouse HSPCs in different regions of the YG8R mouse nervous system. We found substantial engraftment of GFP$^+$ HSPC-derived cells within the DRGs, spinal cord, and peripheral nerves, and as expected, most of the neurons appeared to be myelinated (Fig. 1C and fig. S1). Within the DRGs in all spinal cord regions, donor cells were found in close proximity to neurons and were immunoreactive for the macrophage markers CD68 and major histocompatibility complex class II (MHCII), as well as Iba1, characterizing these cells as DRG-resident macrophages (Fig. 1, C and D, and fig. S2, A and B) (21). In the spinal cord of the recipient YG8R mice, HSPC-derived cells were abundant in the ascending sensory

axon tracts, within the dorsal and ventral roots, motor neuron pools, and dorsal spinal cord gray matter (Fig. 1, C and D). These cells were >99% Iba1^{+} and CD68^{+}, whereas fewer cells expressed MHCII (~30%; fig. S2, A to C), indicating their microglial identity (22, 23). Three-dimensional (3D) visualization of the engrafted spinal cord that was subjected to tissue clearing showed that a high concentration of engrafted HSPC-derived cells was found in close proximity to perivascular regions, suggesting that these cells may have infiltrated the CNS via the vasculature (video S1). Graft-derived cells were also detected throughout the gray and white matter in the brain, brainstem, and cerebellum of transplanted YG8R mice (Fig. 2A). The vast majority (>99%) of HSPC-derived cells within all regions of the brain displayed the typical ramified morphology of microglia and expressed CD68 and Iba1 but were not immunoreactive for MHCII, demonstrating that these cells were microglial cells (Fig. 2B and fig. S2, A, B, and D) (24). Perivascular infiltration in the brain was further demonstrated by the presence of GFP[+] HSPC-derived cells in close proximity to blood vessels (fig. S2E), especially in the highly vascularized choroid plexus (fig. S2F), as previously described (25).

Wild-type mouse HSPC transplantation restores frataxin expression and normalizes mitochondrial function in the brains of YG8R mice

Analysis of murine frataxin (m*Fxn*) expression in the mouse brain confirmed that tissue engraftment of the HSPC-derived cells correlated with partial restoration of m*Fxn* expression in transplanted mice compared to nontransplanted YG8R control mice, although m*Fxn* expression did not reach that of wild-type animals. Residual expression of m*Fxn* was also detected in YG8R mice, most likely because of cross-reactivity of the quantitative polymerase chain reaction (PCR) primers with human *FXN* (Fig. 2C). Mitochondrial dysfunction in FRDA is associated with an increase in oxidized proteins within tissues (10, 26). Compared to wild-type control mice, oxidized proteins were significantly higher ($P < 0.05$) in the cerebrum of YG8R mice and those transplanted with mfxn^{−/−} hFXN[+] HSPCs (Fig. 2D). Wild-type mouse HSPC transplantation resulted in attenuation of the accumulation of oxidized proteins in YG8R mice to amounts comparable to that found in wild-type animals, suggesting restoration of mitochondrial function in the transplanted mice (Fig. 2D).

In addition, mitochondrial function was assessed using mitochondrial PCR array profiling (27) in the cerebrum of wild-type, YG8R, and HSPC-transplanted YG8R mice. Expression of mitochondrial genes crucial for a wide variety of processes ranging from control of apoptosis to oxidative phosphorylation was altered in the YG8R animals. Of the 89 genes tested, 15.7% showed an increase of at least twofold over wild-type mice, whereas only 4.4% of the genes were up-regulated in transplanted YG8R mice (Fig. 2E). Of these genes, five were significantly up-regulated in YG8R mice compared to wild-type animals, including several members of the solute carrier family of inner mitochondrial membrane transporters and other proteins involved in mitochondrial lipid metabolism ($P < 0.05$; Fig. 2E). No significant differences were observed between YG8R mice transplanted with wild-type mouse HSPCs and wild-type animals (Fig. 2E).

Wild-type mouse HSPCs are engrafted in the YG8R mouse heart and muscle, reducing iron deposition and decreasing skeletal muscle atrophy

An increase in oxidized proteins was also demonstrated in the skeletal muscle of YG8R control mice relative to wild-type mice, although this was not significant; normal amounts of oxidized proteins were found in the skeletal muscle of transplanted YG8R mice ($P = 0.0798$; Fig. 3A). Furthermore, in skeletal muscle biopsies, we quantified by mass spectrometry lactate and pyruvate, metabolites that have been shown to be elevated in some mitochondrial diseases (28). There was a significant increase in the lactate-to-pyruvate ratio in the skeletal muscle of YG8R mice compared to wild-type mice ($P < 0.0005$), which was corrected in the HSPC-transplanted YG8R animals (Fig. 3B).

In addition to neurological deficits, FRDA patients also develop a progressive hypertrophic cardiomyopathy (29, 30). Thus, we investigated the potential impact of HSPC transplantation on heart pathology in YG8R mice. However, cardiomyopathy is very mild in this mouse model (10), and no phenotype was found in the YG8R mice compared to wild-type mice at 9 months of age (fig. S3A). Evidence of cellular iron metabolic dysregulation in the form of iron deposition in cardiomyocytes has been observed in FRDA patients (31) and in 14- to 18-month-old YG22 mice (another FRDA mouse model expressing one copy of the mutated human frataxin gene) (10, 32). We observed iron deposition in mouse cardiomyocytes, as revealed by Perl's staining of heart sections from 18-month-old nontransplanted YG8R mice; this deposition was significantly decreased in YG8R mice transplanted with wild-type mouse HSPCs ($P = 0.042$; Fig. 3C).

In both heart and skeletal muscle tissues, m*Fxn* expression was increased in the wild-type HSPC-transplanted mice compared to YG8R control mice (Fig. 3, D and E). Confocal microscopy analysis revealed large numbers of GFP+ cells engrafted in these tissues in HSPC-transplanted YG8R animals (Fig. 3, F and G). The engrafted GFP+ cells expressed CD68 and MHCII (fig. S3, B and C), indicating that these cells were macrophages.

To investigate potential muscular atrophy in YG8R mice, we measured the expression of two muscle-specific E3 ubiquitin ligases, muscle RING finger 1 (MuRF-1) and muscle atrophy F-box/atrogin-1, and a member of the transforming growth factor–β superfamily, myostatin, which are all increased during skeletal muscle atrophy (33, 34). Expression of MuRF-1, atrogin-1, and myostatin was increased in the skeletal muscle from YG8R mice compared to wild-type mice (although this was not significant for atrogin-1). In contrast, expression of these three muscle proteins was normal in the transplanted YG8R mice (Fig. 3H), demonstrating the rescue of this defect by transplantation of wild-type mouse HSPCs.

Macrophages deliver frataxin to YG8R mouse fibroblasts

We previously reported that in the lysosomal storage disorder cystinosis, mouse HSPC-derived macrophages promote functional rescue of diseased cells through a lysosomal corrective mechanism (17). Hence, we asked whether phagocytic cells could also mediate the transfer of frataxin into mfxn$^{-/-}$ hFXN+ mouse fibroblasts in vitro. We cocultured fibroblasts harvested from YG8R mouse neonatal skin with macrophages isolated from the bone marrow of cytochrome c oxidase subunit VIII (Cox8)–GFP DsRed mice that

ubiquitously expressed the mitochon-drial Cox8 protein fused to GFP and the cytosolic DsRed reporter (35, 36). Using live imaging, we observed that the Cox8-GFP protein was transferred from the DsRed-expressing macrophages to the mfxn$^{-/-}$ hFXN$^+$ fibroblasts (Fig. 4A and video S2). In parallel, we used macrophages stably transduced with a lentiviral vector (LV) containing the human mitochondrial frataxin gene tagged with GFP (LV-hFXN-GFP). Mitochondria were then labeled with MitoTracker Red in the coculture assay. Movement of hFXN-GFP–bearing mitochondria was observed from the macrophages to the diseased fibroblasts, and hFXN-GFP could be observed in the recipient FRDA mouse fibroblasts (Fig. 4B and video S3).

Wild-type mouse HSPC-derived microglia and macrophages transfer mitochondrial proteins to YG8R mouse neurons in vivo

To assess whether transfer of mitochondrial proteins occurred in vivo, we transplanted YG8R mice with HPSCs isolated from DsRed Cox8-GFP mice. Cox8-GFP punctae were detected not only within the DsRed-expressing microglial cells but also within neurons in the YG8R mouse brain, spinal cord, and DRGs (Fig. 4C and fig. S4). We typically observed that neurons containing Cox8-GFP were in contact with one or more DsRed$^+$ microglial branch extensions (Fig. 4C), and GFP$^+$ punctae were also observed within these microglial processes (Fig. 4D). Quantification in spinal cord tissue revealed that about 50% of neurons contained Cox8-GFP staining (see Fig. 4E and fig. S5 for quantification methodology). Transfer of frataxin from microglia to neurons was also demonstrated by transplanting YG8R mice with HSPCs isolated from DsRed transgenic mice and stably transduced with LV-hFXN-GFP (Fig. 4F). In addition, evidence of transfer was apparent in the heart and skeletal muscle, in which Cox8-GFP was detected in recipient mouse muscle myocytes that were next to graft-derived macrophages (fig. S4B). Together, these results suggest that mitochondrial protein transfer occurs from microglia to neuronal cells and that this transfer may be involved in HSPC-mediated rescue of the FRDA phenotype in the YG8R mouse model.

DISCUSSION

There is a pressing need to identify effective therapies for FRDA, a debilitating neurodegenerative disease for which there remains no treatment. To date, preclinical studies using stem cells or gene therapy have had limited success or have been restricted to assessment of improvements in specific tissues (29, 37–39). A recent in vivo study reported the prevention and reversal of severe cardiomyopathy in a skeletal muscle conditional frataxin-knockout mouse model after intravenous injection of AAV9 (adeno-associated virus serotype 9)–h*FXN* complementary DNA (cDNA) (29). Here, we demonstrated that a single transplant of wild-type mouse HSPCs into young adult YG8R mice prevented the development of FRDA pathology, including neurobehavioral deficits, muscle weakness, and degeneration of DRG sensory neurons. The key advantage of exogenous HSPC transplantation is the capacity of these cells to permanently repopulate the bone marrow and migrate from their niche to differentiate into phagocytic cell types within multiple tissues (17). HSPCs may even be able to transmigrate across the blood-brain barrier and engraft within the CNS as differentiated microglia (24, 25, 40, 41). This phenomenon is enhanced

by tissue injury (24, 42, 43) or by using busulfan-mediated myeloablation instead of total body irradiation (44). We show that transplanted wild-type mouse HSPCs differentiated into microglial cells in the CNS of the YG8R recipient mice and into macrophages in the DRGs, peripheral nerves, skeletal muscle, and heart, the primary sites of FRDA pathology.

We showed a reduction in oxidative stress in HSPC-treated YG8R mouse tissues compared to that in tissues of YG8R nontransplanted mice or animals transplanted with YG8R HSPCs. Oxidative stress is a major component of FRDA pathogenesis and may account for neuronal degeneration (45). Oxidative stress has also recently been shown to induce DNA damage and elevation of poly(adenosine 5′-diphosphate–ribose) polymerase 1 (PARP1) expression in frataxin-deficient microglial cells, which resulted in increased microglial activation (46). Because PARP1 activation leads to increased inflammatory cytokine expression in microglial cells (47), these findings suggest that oxidative stress may induce neuroinflammatory-mediated neurodegeneration in FRDA. Hence, the robust neurological phenotypic rescue we observed in HSPC-transplanted YG8R mice may be, in part, due to the replacement of the frataxin-deficient microglial cells by wild-type microglia. Mitochondrial function was assessed by mitochondrial PCR array profiling in the cerebrum of YG8R mice. Our findings showed a number of up-regulated genes (>2-fold change) in YG8R mice compared to wild-type mice (13 of 84 genes). In contrast, very few changes in expression were identified between wild-type mice and HSPC-transplanted YG8R mice (four genes), and none was identified with a significant difference. Among the significantly up-regulated genes in YG8R mice versus wild-type mice, there were 25 genes from the solute mitochondrial carrier protein family ($P < 0.05$) (48), including *Mipep*, an important component of the human mitochondrial import machinery implicated in developmental delay (49), and the fatty acid transporter *Cpt1b*, which is up-regulated in posttraumatic stress disorder (50).

Cellular iron metabolism dysregulation was first demonstrated in FRDA by Lamarche and colleagues (31), who reported the presence of iron deposits in cardiomyocytes of patients. Here, we demonstrated the presence of abundant iron deposits in heart sections from nontransplanted YG8R control mice, whereas very few were observed in wild-type mice or YG8R mice transplanted with wild-type mouse HSPCs, suggesting that there was normal iron metabolism in the transplanted YG8R mice. In contrast, preclinical and clinical data using an iron chelator as a potential therapeutic agent showed a limited beneficial effect on some neurological functions but worsening of gait and posture (51).

We propose that a frataxin transfer mechanism is involved in FRDA phenotypic rescue after wild-type mouse HSPC transplantation to YG8R mice. After hFXN-GFP–expressing murine HSPC transplantation into YG8R mice, we observed the transfer of human frataxin-GFP from the mouse HSPC-derived microglia/macrophages to YG8R mouse neurons in the brain, spinal cord, and DRGs and to myocytes in the skeletal muscle and heart. We also demonstrated the transfer of the mitochondrial protein Cox8, suggesting nonselective transfer of mitochondrial proteins. This raises several questions that remain to be answered. First, are entire mitochondria transferred from donor phagocytic cells to neurons or is this transfer limited to mitochondrial proteins? Second, is the main route of transfer through vesicular exchange or intercellular membrane connections? We previously reported that

HSPC-derived macrophages in recipient mouse kidney could deliver cystinosin-containing lysosomes to proximal tubular cells through tunneling nanotubes in a mouse model of cystinosis (17). In this context, tunneling nanotubes crossing the basement membrane of kidney tubular cells seemed to be the only route possible across the continuous, dense tubular basement membrane. The transfer of mitochondria through tunneling nanotubes has been previously shown in vitro in response to cellular stress (52). Here, we showed in vitro that frataxin and Cox8 mitochondrial proteins could be transferred from donor macrophages to frataxin-deficient fibroblasts. In vivo, we observed the mitochondrial proteins frataxin-GFP and Cox8-GFP within recipient YG8R mouse neurons, with about 50% of neurons containing Cox8-GFP in the spinal cord. There are several potential routes for this transfer, including vesicular exchange of genetic material (53), release of mitochondria-containing vesicles (54), or as shown recently, transfer from astrocytes to neurons in a cerebral ischemia mouse model (55). An alternative possibility is the microglia-to-neuron transfer of mitochondria through microglial branch extensions directly in contact with neurons. Microglial processes are dynamic, actively retracting and expanding, and capable of making direct contact with neurons, especially during injury (56, 57).

There are two main limitations to our study. First, the mild delayed cardiac phenotype of YG8R mice fails to accurately reflect FRDA disease progression in human patients. Second, we were unable to demonstrate the route and mechanism of frataxin correction after transplantation in vivo. Further extensive studies with alternative animal models of FRDA will be required before definitive conclusions can be drawn.

Our findings demonstrate that a single infusion of wild-type mouse HSPCs into the YG8R FRDA mouse model resulted in the engraftment and differentiation of these cells into microglia/macrophages in the brain, spinal cord, DRGs, skeletal muscle, and heart, leading to the rescue of the disease phenotype. Our work suggests that this strategy could be a potential approach for treating FRDA.

MATERIALS AND METHODS

Study design

The goals of this study were (i) to investigate whether wild-type mouse HSPC transplantation could prevent progressive deficits in the YG8R mouse model of FRDA, (ii) to determine whether wild-type mouse HSPC transplantation could prevent tissue damage caused by frataxin deficiency, and (iii) to investigate the mechanism by which HSPC-derived cells participated in the rescue of the FRDA phenotype. We transplanted 13 2-month-old YG8R FRDA mice with wild-type mouse HSPCs and compared them to 16 wild-type mice and 4 nontransplanted YG8R FRDA mice. To ensure that neither irradiation nor transplantation was responsible for the improved phenotype observed in the transplanted mice, we also included five YG8R mice transplanted with mouse FRDA HSPCs. Two months after transplantation, we measured donor HSPC engraftment, which ranged between 35 and 96% engraftment. Neurobehavioral testing (open field, rotarod, gait, and grip strength) was performed for all the groups at 5 and 9 months of age by a behavioral core facility in a blinded fashion. Mice were euthanized at 9 months of age, and tissues were collected for cellular, molecular, and histological analyses.

Animals

YG8R mice with a deletion of murine *Fxn* gene (m*Fxn*) and expressing a mutant human *FXN* gene (hFXN) containing 190 + 90 GAA-repeat expansion were generated in a C57BL/6J background, as previously described (10, 58). Breeding pairs consisted of females heterozygous for *Fxn* and males heterozygous for *Fxn* and hemizygous for *FXN* [B6. Cg-Fxntm1Mkn Tg(FXN)YG8Pook/J] and were purchased from the Jackson Laboratory. YG8R and wild-type mice used as controls for these studies were obtained from these breeders. Genotyping was performed using the following primers: mfxn, 5′-CTTCCCTCTACCCTGCCTTC-3′ (forward) and 5′-GGAGAACAGTGGACACAGTAACA-3′ (reverse); PGK-NEO, 5′-CATCGCCTTCTATCGCCTTCT-3′; FXN, 5′-GGGCA-GATAAAGGAAGGAGATAC-3′ (forward) and 5′-ACGATAGGG-CAACACCAATAA-3′ (reverse).

Transgenic mice constitutively expressing GFP [C57BL/6-Tg(ACTB-EGFP)1Osb/J] or DsRed [B6.Cg-Tg(CAG-DsRed*MST) 1Nagy/J] were also purchased from the Jackson Laboratory. The mtGFP-Tg transgenic mice [C57BL/6J-Tg(CAG-Cox8/EGFP)49Rin] expressing the Cox8-GFP mitochondrial fusion protein (35, 36) were provided by the RIKEN BioResource Center through the National BioResource Project of the Ministry of Education, Culture, Sports, Science and Technology (MEXT). mtGFP-Tg mice were backcrossed with DsRed-Tg mice to produce DsRed-mtGFP-Tg mice. Genotyping for mtGFP was carried out by PCR, as previously described (36). Mice were maintained in a temperature- and humidity-controlled animal facility, with a 12-hour light/dark cycle and free access to water and food. Both male and female mice were used in all experiments. All mice were bred at the University of California, San Diego (UCSD) vivarium, and all protocols were approved by the UCSD Institutional Animal Care and Use Committee.

Frataxin-GFP lentivirus construction, production, and titer

The self-inactivating LV, pCCL-EFS-X-WPRE (pCCL)–GFP, was used for stable gene transfer in HSPCs and macrophages. The vector backbone contains the intron-less human elongation factor 1α promoter to drive transgene expression (59, 60). The human FXN cDNA (633 base pairs; clone ID 5300379, GE Healthcare) corresponding to the canonical frataxin (isoform I) found in mitochondria (61) was amplified by PCR using the primers 5′-TTAGGATCCATGTGGACTCTCG-3′ (forward) and 5′-AGAGGATCCAGCATCTTTTCCG-3′ (reverse) and inserted into pCCL-GFP at the Bam HI restriction site in phase with the GFP cDNA. LV was produced and titered as previously described (62).

Bone marrow cell isolation, transduction, transplantation, and engraftment

Bone marrow cells were flushed from the femurs of 6- to 8-week-old YG8R, GFP transgenic, DsRed transgenic, or DsRed mtGFP transgenic mice. HSPCs were isolated by immunomagnetic separation using anti-Sca1 antibody conjugated to magnetic beads (Miltenyi Biotec). Sca1$^+$ cells were directly transplanted by tail vein injection of 1×10^6 cells re-suspended in 100 μl of phosphate-buffered saline (PBS) into lethally irradiated (7 gray; X-Rad 320, PXi) YG8R mice. Before transplantation, Sca1$^+$ cells from the DsRed transgenic mice were first transduced with LV-hFXN-GFP using a multiplicity of infection

(MOI) of 10 in the presence of polybrene (4 mg/ml) in RetroNectin-coated (20 g/ml) 24-well plates at a density of 2×10^6 cells per well for 16 hours in Stem-Span medium (STEMCELL Technologies) supplemented with stem cell factor, thrombopoietin, FLT3 ligand (100 ng/ml each), and interleukin-6 (20 ng/ml) cytokines (PeproTech). Bone marrow cell engraftment of the transplanted cells was measured in peripheral blood 2 months after transplantation; blood samples freshly harvested from the tails were treated with red blood cell lysis buffer (eBioscience) and subsequently analyzed by flow cytometry (BD Accuri C6, BD Biosciences) to determine the proportion of GFP- or DsRed-expressing cells.

Neurobehavioral tests

Wild-type mice, YG8R mice, YG8R mice transplanted with mfxn$^{-/-}$hFXN$^+$ HSPCs, and YG8R mice transplanted with either wild-type mouse GFP or DsRed/mtGFP-labeled HSPCs were tested at both 5 and 9 months of age before being sacrificed for tissue analysis. Rotarod analysis was performed using a Rota-Rod Series 8 apparatus (Ugo Basile). The rod was a knurled plastic dowel (diameter, 6.0 cm) set at a height of 30 cm. During training, the mice were placed on the stationary rotarod for 30 s before the trial was initiated. Then, each mouse was given four trials per day, with a 60-s intertrial interval on the accelerating rotarod (4 to 40 rpm over 5 min). The latency to fall was recorded for each trial. Locomotor activity was measured using an automated monitoring system (Kinder Associates). Polycarbonate cages ($42 \times 22 \times 20$ cm) containing a thin layer of bedding material were placed into frames (25.5×47 cm) mounted with photocell beams. Each mouse was placed into the open field, and all movements were recorded over a 60-s testing period. Grip strength was measured using a device consisting of a 10-cm-long T-shaped bar connected to a digital dynamometer (Ugo Basile). Animals were held by the tail and placed before the bar, allowed to grip the bar with their forelimbs, and then gently pulled backward until the bar was released. Ten consecutive measurements were made for each animal, and both the average and maximal readouts were recorded. Gait measure (stride length) was collected using an automated gait analysis system (CatWalk, Noldus Instruments). Animals were placed at one end of the walkway and allowed to run down the length of the walkway, as two light sources illuminated the surface contact of paws with the glass floor, producing an image of a paw print. During locomotion, the glass walkway was filmed from below by a video camera. The CatWalk software program was used to analyze recorded footage, define individual paw prints (for example, left forepaw and right hindpaw), and give readouts of multiple parameters of gait. Testing was administered daily for 5 days. Only unbroken bouts of locomotion, during which animals ran down the walkway at a consistent speed, were used for analysis.

Primary fibroblast and macrophage isolation and transduction

Fibroblasts were generated from skin biopsies of neonate of YG8R mice. Cultures were maintained using high-glucose Dulbecco's modified Eagle's medium (Life Technologies) supplemented with 10% fetal bovine serum (FBS; Gibco, Life Technologies) and 1% penicillin/streptomycin (PenStrep; Gibco) at 37°C under 5% CO_2. Primary macrophages from DsRed mtGFP mice were derived from bone marrow cells. Bone marrow cells were flushed from the femurs of 6- to 8-week-old mice and kept in culture in RPMI 1640 with 10% FBS, 1% PenStrep, and 10% L929 conditioned medium (29) at 37°C under 5% CO_2.

For macrophage transduction with pCCL-FXN-eGFP, the IC-21 macrophage cell line was used (American Type Culture Collection catalog #TIB-186) and cultured in RPMI 1640 (Gibco). Six-well plates were coated with Retro-Nectin (20 μl/ml; Takara Bio) following the manufacturer's instructions. IC-21 macrophages were plated at a density of 250,000 cells in 2 ml per well and transduced with pCCL-FXN-eGFP using an MOI of 15. Medium was changed 24 hours after transduction.

Live imaging

YG8R fibroblasts were cocultured with DsRed Cox8-GFP or macrophages stably transduced with a lentivirus expressing hFXN-GFP, as previously described (17). Briefly, 75,000 fibroblasts were cocultured with an equal number of macrophages in glass-bottomed culture dishes (MatTek Corp.). hFXN-GFP cocultures were stained with 50 nM MitoTracker (Invitrogen) for 45 min before imaging. Confocal live imaging was performed 1 and 2 days later using PerkinElmer Ultra-View Vox Spinning Disk Confocal with ×40 [numerical aperture (NA), 1.30] and ×60 (NA, 1.42) oil objective at 37°C under 5% CO_2. Images were captured, processed, and analyzed using the Volocity software (PerkinElmer).

Mouse frataxin quantitative reverse transcription PCR

Total RNA was prepared from snap-frozen skeletal muscle, brain, and heart biopsies using the RNeasy Lipid and Fibrous Tissue kits (Qiagen) according to the manufacturer's instructions. cDNA was then prepared using iScript cDNA Synthesis kit (Bio-Rad). Commercial TaqMan probes specific to mouse frataxin were used to quantitate expression (Applied Biosystems).

Measurement of oxidative stress

Protein lysates from tissues directly snap-frozen in liquid nitrogen after dissection were prepared using radioimmunoprecipitation assay buffer (Sigma-Aldrich) containing proteases inhibitors (Roche), as previously described (63). For each assay, 20 μg of protein was used after total protein concentration was determined using bicinchoninic acid (BCA) assay. Proteins were then derivatized by adding 1× 2,4-dinitrophenylhydrazine solution contained in the OxyBlot Protein Oxidation Detection kit (Chemicon International) according to the manufacturer's instructions. Samples were applied to electrophoresis and transferred to a polyvinylidene difluoride membrane. After blocking with 1% BSA/PBS–Tween 20, membrane was incubated with rabbit anti-dinitrophenyl antibody, followed by a goat anti-rabbit horseradish peroxidase conjugate, and visualized using the ECL kit (Pierce). Protein amounts were normalized using an anti-tubulin (ab6161, Abcam) antibody, and band intensity was quantified using the ImagePro software (Media Cybernetics).

Mouse mitochondria RT[2] Profiler PCR Array

RNA was isolated from the cerebrum using the RNeasy Lipid Tissue Mini kit (Qiagen), and 0.5 μg of the sample was then reverse-transcribed with the iScript cDNA Synthesis kit (Bio-Rad). Samples were mixed with SYBR green, equally loaded into all wells of the Mouse Mitochondria RT[2] Profiler PCR Array (catalog no. PAMM-087Z, Qiagen), and amplified as per the manufacturer's recommendation on the CFX96 thermocycler (Bio-Rad). C_t data

were exported, and fold change was calculated using the C_t method between sample genes and a panel of housekeeping controls.

Lactate/pyruvate analysis

Muscle biopsies (10 mg) were homogenized in ice in 1 ml of ice-cold 40% acetonitrile (containing 0.1% formic acid/40% methanol/20% H_2O) using a tissue grinder (Dounce), followed by centrifugation for 10 min at 13,000g. The extraction solution contained a stable isotope of lactate ($^{13}C_3$ sodium lactate, Cambridge Isotope Laboratories Inc.). Supernatants were removed, dried in a SpeedVac/lyophilizer system, and resuspended in 150 μl of 0.1% formic acid. Pellets were redissolved in 0.1 N NAOH, and protein content was measured using BCA assay. Five microliters of each resuspended supernatant was injected on a C18-PFP HPLC column (MAC-MOD Analytical), as previously described (64), and coupled to an API 4000 triple quadrupole mass spectrometer (AB Sciex). Molecular reaction monitoring for lactate (89 > 43), $^{13}C_3$ lactate (92 > 45), and pyruvate (87 > 43 and 87 > 87) was used during the acquisition. Lactate and pyruvate peaks were both normalized to $^{13}C_3$ lactate. Both lactate and pyruvate were further normalized to protein content (in milligrams) before calculation of the final lactate/pyruvate (L/P) peak area ratios used in Fig. 3B. Because the ratio is expressed in terms of normalized peak areas, the ratio values should not be confused with those determined from absolute concentration measurements, as performed in previous studies measuring L/P but still effective for examining relative differences between cohorts.

Vacuole imaging and quantification

DRGs from L5 were collected, sectioned at 30-μm intervals using a cryostat, and mounted on gelatin-coated slides. DRG sections were stained with thionin (Nissl stain) for visualization of neuronal cell bodies. Three DRGs per subject were acquired at a magnification of ×60 using a BZ-X700 fluorescence microscope (Keyence). The presence of vacuoles in each DRG was traced and measured by a blinded experimenter in duplicate using ImageJ; vacuoles were defined as extremely circular white (Nissl-negative) areas with smooth edges within DRG neurons. The number of vacuoles and area of vacuolar space relative to entire area of each DRG section were compared across genotypes.

Heart histology and iron quantification

For histological preparations, terminally anesthetized mice were fixed by intracardial perfusion with 10% formalin. Fixed tissues were dissected, embedded in paraffin wax, and sectioned by standard methods. Sections were deparaffinized and stained using Perl's technique to detect ferric iron, as previously described (10). Whole-heart sections were imaged on an Keyence fluorescence microscope, and a single wide-field image was stitched together. Using the ImagePro Premier software (Media Cybernetics), quantification of iron staining was assessed by isolating the blue channel, measuring the area of signal, and then dividing from the total area of the section. Values were reported normalized to wild type.

Immunofluorescence and image acquisition

Heart and muscle tissues were fixed in 5% paraformaldehyde (PFA), equilibrated in 20% sucrose overnight, and frozen in Tissue-Tek optimal cutting temperature (OCT) medium at −80°C (Sakura Finetek USA); 10-μm sections were cut. The DRG, brain, and spinal cord tissue were fixed in PFA, cryopreserved in 30% sucrose, and frozen in OCT medium. For DRGs, tissue was cut into 20-μm sections and directly mounted to gelatin-coated slides. For the brain and spinal cord, tissue was sectioned to 30 μm and collected as free-floating sections. For immunofluorescence, tissues were incubated with the following antibodies: rat anti-CD68 (1:100; 137001, BioLegend), biotin rat anti-MHCII (1:100; 553622, BD Pharmigen), rabbit anti-GFP (1:500; ab290, Abcam), chicken anti-GFP (1:1500; ab13970, Abcam), rabbit anti-Iba1 (1:1500; #019-19741, Wako), goat anti-mCherry (1:1000; AB0040, Sicgen), mouse anti-NeuN (1:500; MAB377, Millipore), rabbit anti-MBP (1:200; AB980, Millipore), mouse anti-NF200 (1:500; MAB5262, Millipore), mouse anti–α-actinin (1:400; Sigma-Aldrich), rabbit anti–von Willebrand factor (1:300; Chemicon), DAPI (1:500; Molecular Probes), and BODIPY-phalloidin (1:100; Molecular Probes). The appropriate Alexa Fluor–conjugated secondary antibodies (Invitrogen) were used for the visualization of antigens. Images were acquired using an LSM 880 confocal microscope with Airyscan (Zeiss), a Keyence BZ-X710 digital microscope system for high-resolution stitching images of tissue sections, or an Olympus FV1000 confocal microscope for live imaging. Confocal image stacks were analyzed with the Imaris software (Bitplane, Oxford Instruments).

Quantification of neuronal correction

The entire gray matter region of lumbar spinal cord sections from three YG8R mice transplanted with Cox8-GFP HSPCs and an non-transplanted control was stained with NeuN and imaged at 20× on an LSM 880 confocal microscope (Zeiss). NeuN+ neuronal cells were outlined and counted using the ImagePro Plus software (Media Cybernetics) and then assessed for GFP positivity, which was reported as a percentage of total NeuN cells (fig. S4). All acquisition, filtration, and processing steps were performed identically on the GFP channel between all samples.

Optical clearing of mouse spinal cord

A 6-mm segment of the cervical spinal cord from a mouse at 3 months after transplantation with DsRed+ HSPCs was processed for optical clearing, as previously described (65). Briefly, PFA-fixed tissue was infused with hydrogel monomer solution (4% PFA, 4% acrylamide, and 0.05% bis-acrylamide) and was thermally polymerized. Lipids were then passively extracted in SDS-containing borate buffer at 37°C for 4 weeks until the tissue was cleared. Clarified tissue was incubated in RapiClear CS for 1 day and mounted using a WillCo dish. Tissues were then imaged using an Olympus FV1200 system equipped with a 10× water immersion objective (NA, 0.6; working distance, 3 mm; stack size, 1.65 mm; step size, 5 μm).

Statistics

We did not exclude any animals from our experiments. Experimenters were blinded to the genotype of the specific sample to every extent possible. We did not perform any power

calculation analysis. All data displayed normal variance, except DRG vacuole measurements. For normal data and mitochondrial PCR array data, we performed one-way ANOVA, followed by post hoc Student's *t* test, to determine the statistical significance using GraphPad Prism 7.01 (GraphPad Software). Oxidative stress measurements used one-tailed *t* tests with the assumption that YG8R mouse tissue oxidation would be higher. For vacuole measurements, we used the Mann-Whitney nonparametric test corrected for multiple testing by the Bonferroni correction. In vitro experiments were performed in biological triplicates. Error bars denote SEM. Significance is indicated as follows: $*P < 0.05$, $**P < 0.005$, and $***P < 0.0005$.

Supplementary Material

Refer to Web version on PubMed Central for supplementary material.

Acknowledgments

REFERENCES AND NOTES

1. Campuzano V, Montermini L, Moltò MD, Pianese L, Cossée M, Cavalcanti F, Monros E, Rodius F, Duclos F, Monticelli A, Zara F, Cañizares J, Koutnikova H, Bidichandani SI, Gellera C, Brice A, Trouillas P, De Michele G, Filla A, De Frutos R, Palau F, Patel PI, Di Donato S, Mandel JL, Cocozza S, Koenig M, Pandolfo M. Friedreich's ataxia: Autosomal recessive disease caused by an intronic GAA triplet repeat expansion. Science. 1996; 271:1423–1427. [PubMed: 8596916]

2. Koutnikova H, Campuzano V, Foury F, Dollé P, Cazzalini O, Koenig M. Studies of human, mouse and yeast homologues indicate a mitochondrial function for frataxin. Nat Genet. 1997; 16:345–351. [PubMed: 9241270]

3. Adinolfi S, Iannuzzi C, Prischi F, Pastore C, Iametti S, Martin SR, Bonomi F, Pastore A. Bacterial frataxin CyaY is the gatekeeper of iron-sulfur cluster formation catalyzed by IscS. Nat Struct Mol Biol. 2009; 16:390–396. [PubMed: 19305405]

4. Cook JD, Bencze KZ, Jankovic AD, Crater AK, Busch CN, Bradley PB, Stemmler AJ, Spaller MR, Stemmler TL. Monomeric yeast frataxin is an iron-binding protein. Biochemistry. 2006; 45:7767–7777. [PubMed: 16784228]

5. Gakh O, Park S, Liu G, Macomber L, Imlay JA, Ferreira GC, Isaya G. Mitochondrial iron detoxification is a primary function of frataxin that limits oxidative damage and preserves cell longevity. Hum Mol Genet. 2006; 15:467–479. [PubMed: 16371422]

6. Parkinson MH, Boesch S, Nachbauer W, Mariotti C, Giunti P. Clinical features of Friedreich's ataxia: Classical and atypical phenotypes. J Neurochem. 2013; 126(suppl 1):103–117. [PubMed: 23859346]

7. Pandolfo M. Friedreich ataxia: The clinical picture. J Neurol. 2009; 256(suppl 1):3–8.

8. Koeppen AH, Mazurkiewicz JE. Friedreich ataxia: Neuropathology revised. J Neuropathol Exp Neurol. 2013; 72:78–90. [PubMed: 23334592]

9. Solbach K, Kraff O, Minnerop M, Beck A, Schöls L, Gizewski ER, Ladd ME, Timmann D. Cerebellar pathology in Friedreich's ataxia: Atrophied dentate nuclei with normal iron content. Neuroimage Clin. 2014; 6:93–99. [PubMed: 25379420]

10. Al-Mahdawi S, Pinto RM, Varshney D, Lawrence L, Lowrie MB, Hughes S, Webster Z, Blake J, Cooper JM, King R, Pook MA. GAA repeat expansion mutation mouse models of Friedreich ataxia exhibit oxidative stress leading to progressive neuronal and cardiac pathology. Genomics. 2006; 88:580–590. [PubMed: 16919418]

11. Anjomani Virmouni S, Ezzatizadeh V, Sandi C, Sandi M, Al-Mahdawi S, Chutake Y, Pook MA. A novel GAA-repeat-expansion-based mouse model of Friedreich's ataxia. Dis Model Mech. 2015; 8:225–235. [PubMed: 25681319]

12. Anjomani Virmouni S, Sandi C, Al-Mahdawi S, Pook MA. Cellular, molecular and functional characterisation of YAC transgenic mouse models of Friedreich ataxia. PLOS ONE. 2014; 9:e107416. [PubMed: 25198290]

13. Gaide Chevronnay HP, Janssens V, Van Der Smissen P, Rocca CJ, Liao XH, Refetoff S, Pierreux CE, Cherqui S, Courtoy PJ. Hematopoietic stem cells transplantation can normalize thyroid function in a cystinosis mouse model. Endocrinology. 2016; 157:1363–1371. [PubMed: 26812160]

14. Rocca CJ, Kreymerman A, Ur SN, Frizzi KE, Naphade S, Lau A, Tran T, Calcutt NA, Goldberg JL, Cherqui S. Treatment of inherited eye defects by systemic hematopoietic stem cell transplantation. Invest Ophthalmol Vis Sci. 2015; 56:7214–7223. [PubMed: 26540660]

15. Syres K, Harrison F, Tadlock M, Jester JV, Simpson J, Roy S, Salomon DR, Cherqui S. Successful treatment of the murine model of cystinosis using bone marrow cell transplantation. Blood. 2009; 114:2542–2552. [PubMed: 19506297]

16. Yeagy BA, Harrison F, Gubler MC, Koziol JA, Salomon DR, Cherqui S. Kidney preservation by bone marrow cell transplantation in hereditary nephropathy. Kidney Int. 2011; 79:1198–1206. [PubMed: 21248718]

17. Naphade S, Sharma J, Gaide Chevronnay HP, Shook MA, Yeagy BA, Rocca CJ, Ur SN, Lau AJ, Courtoy PJ, Cherqui S. Brief reports: Lysosomal cross-correction by hematopoietic stem cell-derived macrophages via tunneling nanotubes. Stem Cells. 2015; 33:301–309. [PubMed: 25186209]

18. Domhan S, Ma L, Tai A, Anaya Z, Beheshti A, Zeier M, Hlatky L, Abdollahi A. Intercellular communication by exchange of cytoplasmic material via tunneling nano-tube like structures in primary human renal epithelial cells. PLOS ONE. 2011; 6:e21283. [PubMed: 21738629]

19. Sisakhtnezhad S, Khosravi L. Emerging physiological and pathological implications of tunneling nanotubes formation between cells. Eur J Cell Biol. 2015; 94:429–443. [PubMed: 26164368]

20. Vallabhaneni KC, Haller H, Dumler I. Vascular smooth muscle cells initiate proliferation of mesenchymal stem cells by mitochondrial transfer via tunneling nanotubes. Stem Cells Dev. 2012; 21:3104–3113. [PubMed: 22676452]

21. Ton BHT, Chen Q, Gaina G, Tucureanu C, Georgescu A, Strungaru C, Flonta ML, Sah D, Ristoiu V. Activation profile of dorsal root ganglia Iba-1 (+) macrophages varies with the type of lesion in rats. Acta Histochem. 2013; 115:840–850. [PubMed: 23701965]

22. Romero A, Romero-Alejo E, Vasconcelos N, Puig MM. Glial cell activation in the spinal cord and dorsal root ganglia induced by surgery in mice. Eur J Pharmacol. 2013; 702:126–134. [PubMed: 23396227]

23. Schmitt AB, Brook GA, Buss A, Nacimiento W, Noth J, Kreutzberg GW. Dynamics of microglial activation in the spinal cord after cerebral infarction are revealed by expression of MHC class II antigen. Neuropathol Appl Neurobiol. 1998; 24:167–176. [PubMed: 9717181]

24. Priller J, Flügel A, Wehner T, Boentert M, Haas CA, Prinz M, Fernández-Klett F, Prass K, Bechmann I, de Boer BA, Frotscher M, Kreutzberg GW, Persons DA, Dirnagl U. Targeting gene-modified hematopoietic cells to the central nervous system: Use of green fluorescent protein uncovers microglial engraftment. Nat Med. 2001; 7:1356–1361. [PubMed: 11726978]

25. Eglitis MA, Mezey É. Hematopoietic cells differentiate into both microglia and macroglia in the brains of adult mice. Proc Natl Acad Sci USA. 1997; 94:4080–4085. [PubMed: 9108108]

26. Schulz JB, Dehmer T, Schöls L, Mende H, Hardt C, Vorgerd M, Bürk K, Matson W, Dichgans J, Beal MF, Bogdanov MB. Oxidative stress in patients with Friedreich ataxia. Neurology. 2000; 55:1719–1721. [PubMed: 11113228]

27. Kim J, Moody JP, Edgerly CK, Bordiuk OL, Cormier K, Smith K, Beal MF, Ferrante RJ. Mitochondrial loss, dysfunction and altered dynamics in Huntington's disease. Hum Mol Genet. 2010; 19:3919–3935. [PubMed: 20660112]

28. Robinson BH. Lactic acidemia and mitochondrial disease. Mol Genet Metab. 2006; 89:3–13. [PubMed: 16854608]

29. Perdomini M, Belbellaa B, Monassier L, Reutenauer L, Messaddeq N, Cartier N, Crystal RG, Aubourg P, Puccio H. Prevention and reversal of severe mitochondrial cardiomyopathy by gene therapy in a mouse model of Friedreich's ataxia. Nat Med. 2014; 20:542–547. [PubMed: 24705334]

30. Weidemann F, Störk S, Liu D, Hu K, Herrmann S, Ertl G, Niemann M. Cardiomyopathy of Friedreich ataxia. J Neurochem. 2013; 126(suppl 1):88–93. [PubMed: 23859344]

31. Lamarche JB, Côté M, Lemieux B. The cardiomyopathy of Friedreich's ataxia morphological observations in 3 cases. Can J Neurol Sci. 1980; 7:389–396. [PubMed: 6452194]

32. Puccio H, Simon D, Cossée M, Criqui-Filipe P, Tiziano F, Melki J, Hindelang C, Matyas R, Rustin P, Koenig M. Mouse models for Friedreich ataxia exhibit cardiomyopathy, sensory nerve defect and Fe-S enzyme deficiency followed by intramitochondrial iron deposits. Nat Genet. 2001; 27:181–186. [PubMed: 11175786]

33. Bodine SC, Baehr LM. Skeletal muscle atrophy and the E3 ubiquitin ligases MuRF1 and MAFbx/atrogin-1. Am J Physiol Endocrinol Metab. 2014; 307:E469–E484. [PubMed: 25096180]

34. Rodriguez J, Vernus B, Chelh I, Cassar-Malek I, Gabillard JC, Hadj Sassi A, Seiliez I, Picard B, Bonnieu A. Myostatin and the skeletal muscle atrophy and hypertrophy signaling pathways. Cell Mol Life Sci. 2014; 71:4361–4371. [PubMed: 25080109]

35. Shitara H, Shimanuki M, Hayashi JI, Yonekawa H. Global imaging of mitochondrial morphology in tissues using transgenic mice expressing mitochondrially targeted enhanced green fluorescent protein. Exp Anim. 2010; 59:99–103. [PubMed: 20224174]

36. Shitara H, Kaneda H, Sato A, Iwasaki K, Hayashi JI, Taya C, Yonekawa H. Non-invasive visualization of sperm mitochondria behavior in transgenic mice with introduced green fluorescent protein (GFP). FEBS Lett. 2001; 500:7–11. [PubMed: 11434917]

37. Lim F, Palomo GM, Mauritz C, Giménez-Cassina A, Illana B, Wandosell F, Díaz-Nido J. Functional recovery in a Friedreich's ataxia mouse model by frataxin gene transfer using an HSV-1 amplicon vector. Mol Ther. 2007; 15:1072–1078. [PubMed: 17375064]

38. Vyas PM, Tomamichel WJ, Pride PM, Babbey CM, Wang Q, Mercier J, Martin EM, Payne RM. A TAT–frataxin fusion protein increases lifespan and cardiac function in a conditional Friedreich's ataxia mouse model. Hum Mol Genet. 2012; 21:1230–1247. [PubMed: 22113996]

39. Jones J, Estirado A, Redondo C, Pacheco-Torres J, Sirerol-Piquer MS, Garcia-Verdugo JM, Martinez S. Mesenchymal stem cells improve motor functions and decrease neurodegeneration in ataxic mice. Mol Ther. 2015; 23:130–138. [PubMed: 25070719]

40. Brazelton TR, Rossi FMV, Keshet GI, Blau HM. From marrow to brain: Expression of neuronal phenotypes in adult mice. Science. 2000; 290:1775–1779. [PubMed: 11099418]

41. Mezey É, Chandross KJ, Harta G, Maki RA, McKercher SR. Turning blood into brain: Cells bearing neuronal antigens generated in vivo from bone marrow. Science. 2000; 290:1779–1782. [PubMed: 11099419]

42. Rennert RC, Sorkin M, Garg RK, Gurtner GC. Stem cell recruitment after injury: Lessons for regenerative medicine. Regen Med. 2012; 7:833–850. [PubMed: 23164083]

43. Borlongan CV, Glover LE, Tajiri N, Kaneko Y, Freeman TB. The great migration of bone marrow-derived stem cells toward the ischemic brain: Therapeutic implications for stroke and other neurological disorders. Prog Neurobiol. 2011; 95:213–228. [PubMed: 21903148]

44. Wilkinson FL, Sergijenko A, Langford-Smith KJ, Malinowska M, Wynn RF, Bigger BW. Busulfan conditioning enhances engraftment of hematopoietic donor-derived cells in the brain compared with irradiation. Mol Ther. 2013; 21:868–876. [PubMed: 23423338]

45. Yokota T, Igarashi K, Uchihara T, Jishage K-i, Tomita H, Inaba A, Li Y, Arita M, Suzuki H, Mizusawa H, Arai H. Delayed-onset ataxia in mice lacking α-tocopherol transfer protein: Model for neuronal degeneration caused by chronic oxidative stress. Proc Natl Acad Sci USA. 2001; 98:15185–15190. [PubMed: 11752462]

46. Shen Y, McMackin MZ, Shan Y, Raetz A, David S, Cortopassi G. Frataxin deficiency promotes excess microglial DNA damage and inflammation that is rescued by PJ34. PLOS ONE. 2016; 11:e0151026. [PubMed: 26954031]

47. Martínez-Zamudio RI, Ha HC. PARP1 enhances inflammatory cytokine expression by alteration of promoter chromatin structure in microglia. Brain Behav. 2014; 4:552–565. [PubMed: 25161822]

48. Palmieri F. The mitochondrial transporter family (SLC25): Physiological and pathological implications. Pflugers Arch. 2004; 447:689–709. [PubMed: 14598172]

49. Eldomery MK, Akdemir ZC, Vögtle F-N, Charng W-L, Mulica P, Rosenfeld JA, Gambin T, Gu S, Burrage LC, Al Shamsi A, Penney S, Jhangiani SN, Zimmerman HH, Muzny DM, Wang X, Tang J, Medikonda R, Ramachandran PV, Wong L-J, Boerwinkle E, Gibbs RA, Eng CM, Lalani SR, Hertecant J, Rodenburg RJ, Abdul-Rahman OA, Yang Y, Xia F, Wang MC, Lupski JR, Meisinger C, Sutton VR. MIPEP recessive variants cause a syndrome of left ventricular non-compaction, hypotonia and infantile death. Genome Med. 2016; 8:106. [PubMed: 27799064]

50. Zhang L, Li H, Hu X, Benedek DM, Fullerton CS, Forsten RD, Naifeh JA, Li X, Wu H, Benevides KN, Le T, Smerin S, Russell DW, Ursano RJ. Mitochondria-focused gene expression profile reveals common pathways and CPT1B dysregulation in both rodent stress model and human subjects with PTSD. Transl Psychiatry. 2015; 5:e580. [PubMed: 26080315]

51. Pandolfo M, Hausmann L. Deferiprone for the treatment of Friedreich's ataxia. J Neurochem. 2013; 126(suppl 1):142–146. [PubMed: 23859349]

52. Liu K, Ji K, Guo L, Wu W, Lu H, Shan P, Yan C. Mesenchymal stem cells rescue injured endothelial cells in an in vitro ischemia–reperfusion model via tunneling nanotube like structure-mediated mitochondrial transfer. Microvasc Res. 2014; 92:10–18. [PubMed: 24486322]

53. Ridder K, Keller S, Dams M, Rupp AK, Schlaudraff J, Del Turco D, Starmann J, Macas J, Karpova D, Devraj K, Depboylu C, Landfried B, Arnold B, Plate KH, Höglinger G, Sültmann H, Altevogt P, Momma S. Extracellular vesicle-mediated transfer of genetic information between the hematopoietic system and the brain in response to inflammation. PLOS Biol. 2014; 12:e1001874. [PubMed: 24893313]

54. Islam MN, Das SR, Emin MT, Wei M, Sun L, Westphalen K, Rowlands DJ, Quadri SK, Bhattacharya S, Bhattacharya J. Mitochondrial transfer from bone-marrow–derived stromal cells to pulmonary alveoli protects against acute lung injury. Nat Med. 2012; 18:759–765. [PubMed: 22504485]

55. Hayakawa K, Esposito E, Wang X, Terasaki Y, Liu Y, Xing C, Ji X, Lo EH. Transfer of mitochondria from astrocytes to neurons after stroke. Nature. 2016; 535:551–555. [PubMed: 27466127]

56. Tremblay M-È, Lowery RL, Majewska AK. Microglial interactions with synapses are modulated by visual experience. PLOS Biol. 2010; 8:e1000527. [PubMed: 21072242]

57. Wake H, Moorhouse AJ, Jinno S, Kohsaka S, Nabekura J. Resting microglia directly monitor the functional state of synapses in vivo and determine the fate of ischemic terminals. J Neurosci. 2009; 29:3974–3980. [PubMed: 19339593]

58. Al-Mahdawi S, Pinto RM, Ruddle P, Carroll C, Webster Z, Pook M. GAA repeat instability in Friedreich ataxia YAC transgenic mice. Genomics. 2004; 84:301–310. [PubMed: 15233994]

59. Dull T, Zufferey R, Kelly M, Mandel RJ, Nguyen M, Trono D, Naldini L. A third-generation lentivirus vector with a conditional packaging system. J Virol. 1998; 72:8463–8471. [PubMed: 9765382]

60. Zychlinski D, Schambach A, Modlich U, Maetzig T, Meyer J, Grassman E, Mishra A, Baum C. Physiological promoters reduce the genotoxic risk of integrating gene vectors. Mol Ther. 2008; 16:718–725. [PubMed: 18334985]

61. Pérez-Luz S, Gimenez-Cassina A, Fernández-Frías I, Wade-Martins R, Diaz-Nido J. Delivery of the 135 kb human frataxin genomic DNA locus gives rise to different frataxin isoforms. Genomics. 2015; 106:76–82. [PubMed: 26027909]

62. Harrison F, Yeagy BA, Rocca CJ, Kohn DB, Salomon DR, Cherqui S. Hematopoietic stem cell gene therapy for the multisystemic lysosomal storage disorder cystinosis. Mol Ther. 2013; 21:433–444. [PubMed: 23089735]

63. Campuzano V, Montermini L, Lutz Y, Cova L, Hindelang C, Jiralerspong S, Trottier Y, Kish SJ, Faucheux B, Trouillas P, Authier FJ, Dürr A, Mandel JL, Vescovi A, Pandolfo M, Koenig M. Frataxin is reduced in Friedreich ataxia patients and is associated with mitochondrial membranes. Hum Mol Genet. 1997; 6:1771–1780. [PubMed: 9302253]

64. Gertsman I, Gangoiti JA, Barshop BA. Validation of a dual LC-HRMS platform for clinical metabolic diagnosis in serum, bridging quantitative analysis and untargeted metabolomics. Metabolomics. 2014; 10:312–323. [PubMed: 25411574]

65. Chung K, Wallace J, Kim SY, Kalyanasundaram S, Andalman AS, Davidson TJ, Mirzabekov JJ, Zalocusky KA, Mattis J, Denisin AK, Pak S, Bernstein H, Ramakrishnan C, Grosenick L, Gradinaru V, Deisseroth K. Structural and molecular interrogation of intact biological systems. Nature. 2013; 497:332–337. [PubMed: 23575631]
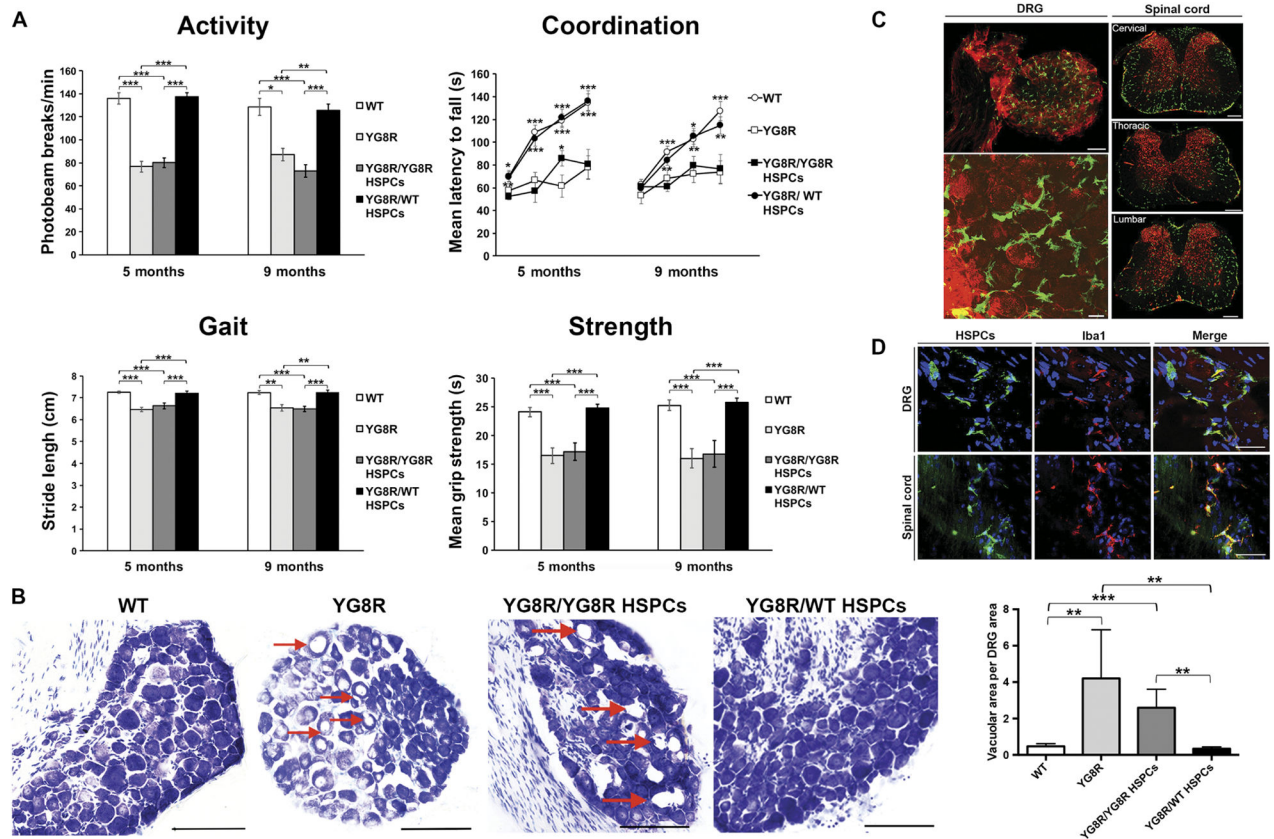
Fig. 1. Neurobehavioral testing in YG8R mice transplanted with wild-type mouse HSPCs
(**A**) Neurobehavioral testing (open field, rotarod, gait, and grip strength) was performed for wild-type (WT) mice ($n = 16$), nontransplanted YG8R control mice (YG8R; $n = 4$), YG8R mice transplanted with YG8R mfxn$^{-/-}$ hFXN$^+$ HSPCs (YG8R/ YG8R HSPCs; $n = 5$), and YG8R mice transplanted with wild-type HSPCs (YG8R/WT HSPCs; $n = 13$) at both 5 and 9 months of age. Locomotor activity was tested using an open-field test, coordination was tested using a rotarod test, gait was tested using an automated gait analysis system, and muscle strength was tested using a forelimb grip strength test. Data are means ± SEM. *$P <$ 0.05, **$P <$ 0.005 and ***$P <$ 0.0005. For statistical comparison of three experimental groups, a mixed analysis of variance (ANOVA) with age of testing as a within-subjects variable was used, followed by independent sample t test. (**B**) Nissl-stained sections of the lumbar DRGs (L5) from representative 9-month-old wild-type mice ($n = 15$), YG8R control mice ($n = 4$), YG8R/YG8R HSPCs ($n = 4$), and YG8R/WT HSPCs ($n = 11$). Large vacuoles are shown by red arrows. Scale bars, 100 μm. Graph depicts total vacuolar area per DRG area (right). Data are means ± SEM. **$P <$ 0.005 and ***$P <$ 0.0005 (Mann-Whitney non-parametric test corrected for multiple testing by the Bonferroni correction). (**C**) Representative confocal images from a WT GFP$^+$ HSPC-transplanted YG8R mouse 7 months after transplantation, stained with anti-GFP (green) and anti-NeuN (red) antibodies. Left: Image of a DRG. Scale bar, 100 μm (top). Magnified image with scale bar, 20 μm (below). Right: Images of cervical, thoracic, and lumbar spinal cord. Scale bars, 250 μm. (**D**) Confocal images of the DRG and spinal cord from a YG8R mouse transplanted with GFP$^+$

HSPCs show engrafted cells (GFP; green) with neurons (NeuN; blue) and the Iba1 microglial marker (red). Scale bars, 30 μm.
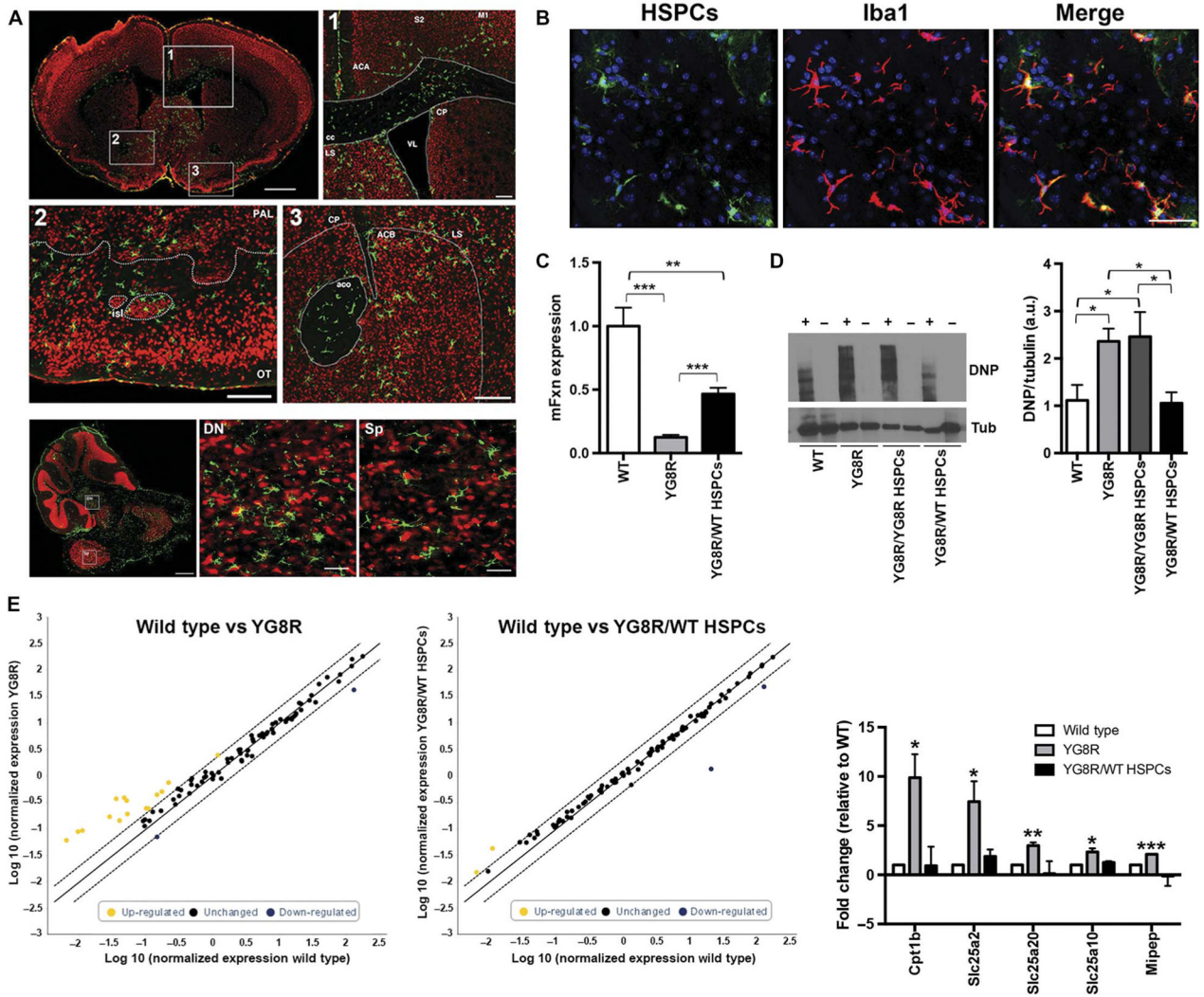
Fig. 2. Transplanted wild-type mouse HSPCs engraft throughout the YG8R mouse brain
(**A**) Representative transverse section of the brain of a YG8R mouse 7 months after
transplantation with wild-type mouse GFP+ HSPCs, labeled with anti-GFP (green) and anti-
NeuN (red) antibodies. Scale bar, 1 mm. Magnified image #1 of the brain shows the
periventricular regions including the corpus callosum (cc), lateral septal nuclei (LS), caudate
putamen (CP), anterior cingulate area (ACA), and the somatosensory cortex (M1 and S2).
VL, lateral ventricle. Scale bar, 150 μm. Magnified image #2 of the mouse brain shows the
ventral striatum including the anterior commissure (aco), nucleus accumbens (ACB), lateral
septal nuclei, and caudate putamen. Scale bar, 150 μm. Magnified image #3 shows the
ventral pallidum (PAL) and the ventral striatum, including the islands of Calleja (isl) and the
olfactory tubercle (OT). Scale bar, 150 μm. Lower panels depict the gray and white matter of
the brain stem and cerebellum. Scale bar, 500 μm. Insets magnify the dentate nucleus (DN)
of the cerebellum and the spinal trigeminal nucleus (Sp) of the brain stem. Scale bar, 50 μm.
(**B**) Confocal images of YG8R mouse brain labeled with anti-GFP (green), anti-Iba1 (red),
and anti-NeuN (blue) antibodies. Scale bar, 30 μm. (**C**) Quantification of murine frataxin
mRNA expression in the cerebellum from wild-type mice ($n = 14$), YG8R mice ($n = 8$), and

YG8R mice transplanted with wild-type mouse HSPCs ($n = 13$). Data are represented as fold change relative to wild type normalized to glyceraldehyde-3-phosphate dehydrogenase (GAPDH). Data are means ± SEM. **P < 0.005 and ***P < 0.0005 (one-way ANOVA, followed by post hoc Student's *t* test). (**D**) Representative Western blot showing protein oxidation in the cerebrum from one wild-type mouse, one YG8R nontransplanted mouse, one YG8R mouse transplanted with YG8R HSPCs (YG8R/YG8R HSPCs), and one YG8R mouse transplanted with wild-type HSPCs (YG8R/WT HSPCs), with (+) or without (−) a 2,4-dinitrophenylhydrazine (DNP) derivatization reagent. Cerebrum tissue from 9-month-old YG8R control mice ($n = 4$) and YG8R/YG8R HSPC mice ($n = 4$) was compared to that from wild-type mice ($n = 6$) and YG8R/WT HSPCs ($n = 6$). Data are means ± SEM. *P < 0.05 (one-tailed *t* test). Tub, tubulin; a.u., arbitrary units. (**E**) Scatterplots of mitochondrial gene expression changes in the cerebrum ($n = 3$) from wild-type animals compared to YG8R nontransplanted control mice (left) or YG8R/WT HSPCs mice (middle). The center line represents no change in gene expression, and up-regulated and down-regulated genes at a fold change of 2 or greater are noted by yellow and blue dots, respectively. mRNA changes that are significantly different between groups are represented on a separate bar graph (right). Data are means ± SEM. *P < 0.05, **P < 0.005, ***P < 0.0005, compared to wild-type mice (one-way ANOVA, followed by post hoc Student's *t* test).
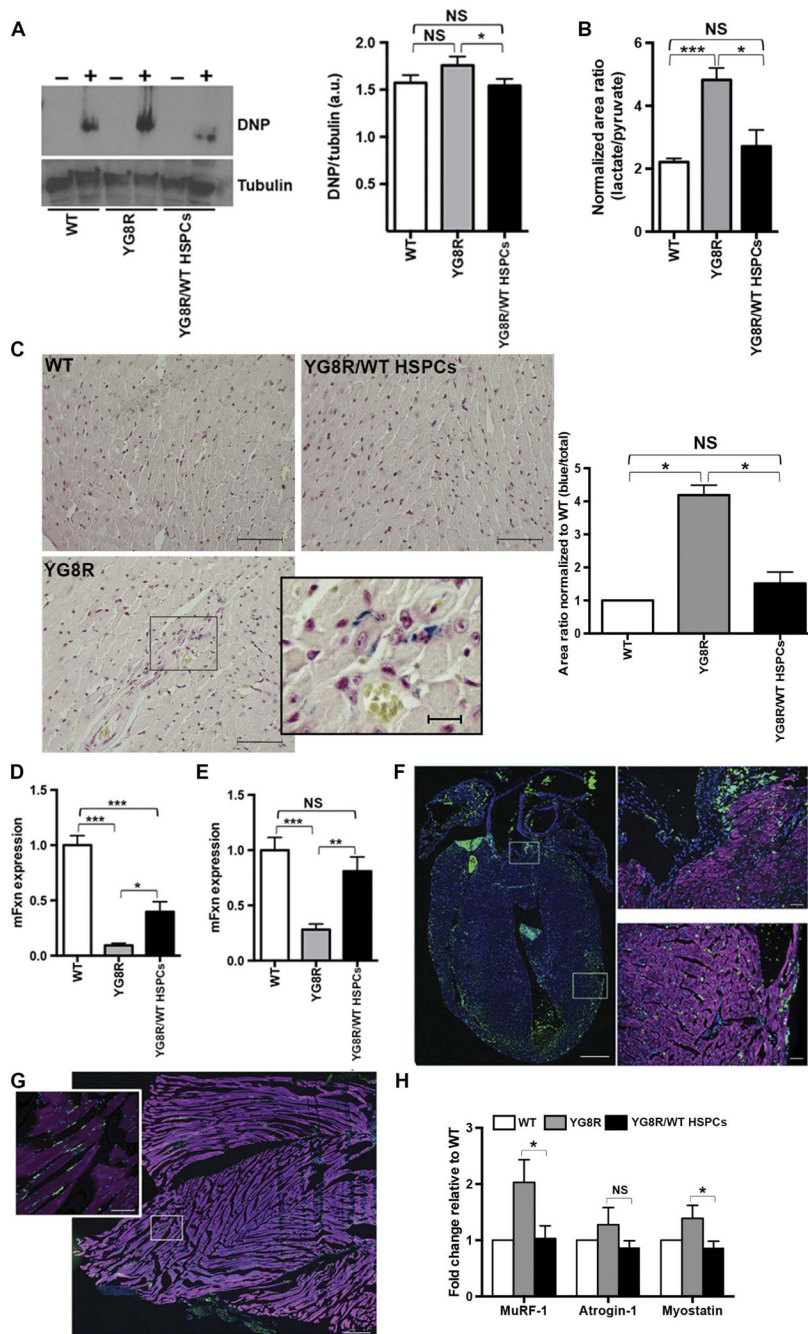
Fig. 3. Transplanted wild-type mouse HSPCs are engrafted in the heart and muscle of YG8R recipient mice

(**A**) Representative Western blot showing protein oxidation in the skeletal muscle of one wild-type mouse, one YG8R control mouse (YG8R), and one YG8R mouse transplanted with wild-type mouse HSPCs (YGR8/WT HSPCs), with (+) or without (−) a 2,4-dinitrophenylhydrazine derivatization reagent. Nine-month-old YG8R control mice [which included nontransplanted YG8R mice ($n = 4$) and YG8R mice transplanted with YG8R HSPCs ($n = 5$)] were compared to wild-type mice ($n = 16$) and YG8R mice transplanted with wild-type mouse HSPCs (YG8R/WT HSPCs; $n = 13$). Error bars indicate SEM. *$P <$

0.05. NS, statistically nonsignificant (one-tailed t test). (**B**) Quantification of lactate and pyruvate by mass spectrometry (represented as a ratio) in muscle tissues from wild-type mice ($n = 6$), YG8R nontransplanted control mice ($n = 3$), and YG8R mice transplanted with wild-type mouse HSPCs ($n = 5$). Error bars indicate SEM. *$P < 0.05$ and ***$P < 0.0005$ (one-way ANOVA, followed by post hoc Student's t test). (**C**) Representative Perl's staining of heart sections from an 18-month-old wild-type mouse, YG8R nontransplanted mouse, and YG8R mouse transplanted with wild-type HSPCs; blue staining indicates iron deposition. Scale bars, 50 and 15 μm (inset). The associated bar graph shows iron quantification in heart sections from wild-type mice ($n = 4$), YG8R control mice [nontransplanted ($n = 2$) and YG8R mice transplanted with YG8R HSPCs ($n = 2$)], and YG8R mice transplanted with wild-type mouse HSPCs ($n = 3$). Error bars indicate SEM. *$P < 0.05$ (one-way ANOVA, followed by post hoc Student's t test). (**D** and **E**) Quantification of murine frataxin mRNA expression in the heart (D) and skeletal muscle (E) from wild-type mice ($n = 12$), YG8R nontransplanted control mice (YG8R; $n = 7$), and YG8R mice transplanted with wild-type mouse HSPCs (YG8R/WT HSPCs; $n = 11$). Data are represented as fold change relative to wild-type normalized to GAPDH; error bars indicate SEM. *$P < 0.05$, **$P < 0.005$, ***$P < 0.0005$ (one-way ANOVA, followed by post hoc Student's t test). (**F**) Heart section from a YG8R mouse 7 months after transplantation with wild-type mouse HSPCs, stained with anti-GFP (green) antibody, the cardiomyocyte marker anti–α-actinin (magenta) antibody, and 4′,6-diamidino-2-phenylindole (DAPI) nuclear stain (blue). Scale bar, 150 μm. Magnified images on the right show the left ventricle (bottom) and the base of the aorta (top). Scale bars, 50 μm. (**G**) Skeletal muscle section from a YG8R mouse 7 months after transplantation with wild-type mouse HSPCs, stained with anti-GFP (green) antibody, filamentous actin dye phalloidin (magenta) antibody, and DAPI nuclear stain (blue). Scale bar, 150 μm. Magnified image of the skeletal muscle (inset). Scale bar, 50 μm. (**H**) Quantification of murine MuRF-1, atrogin-1, and myostatin mRNA expression in the skeletal muscle from wild-type mice ($n = 5$), YG8R nontransplanted control mice ($n = 5$), and YG8R mice transplanted with wild-type mouse HSPCs ($n = 5$). Data are represented as fold change relative to wild-type normalized to GAPDH; error bars indicate SEM. *$P < 0.05$ (one-way ANOVA, followed by post hoc Student's t test).
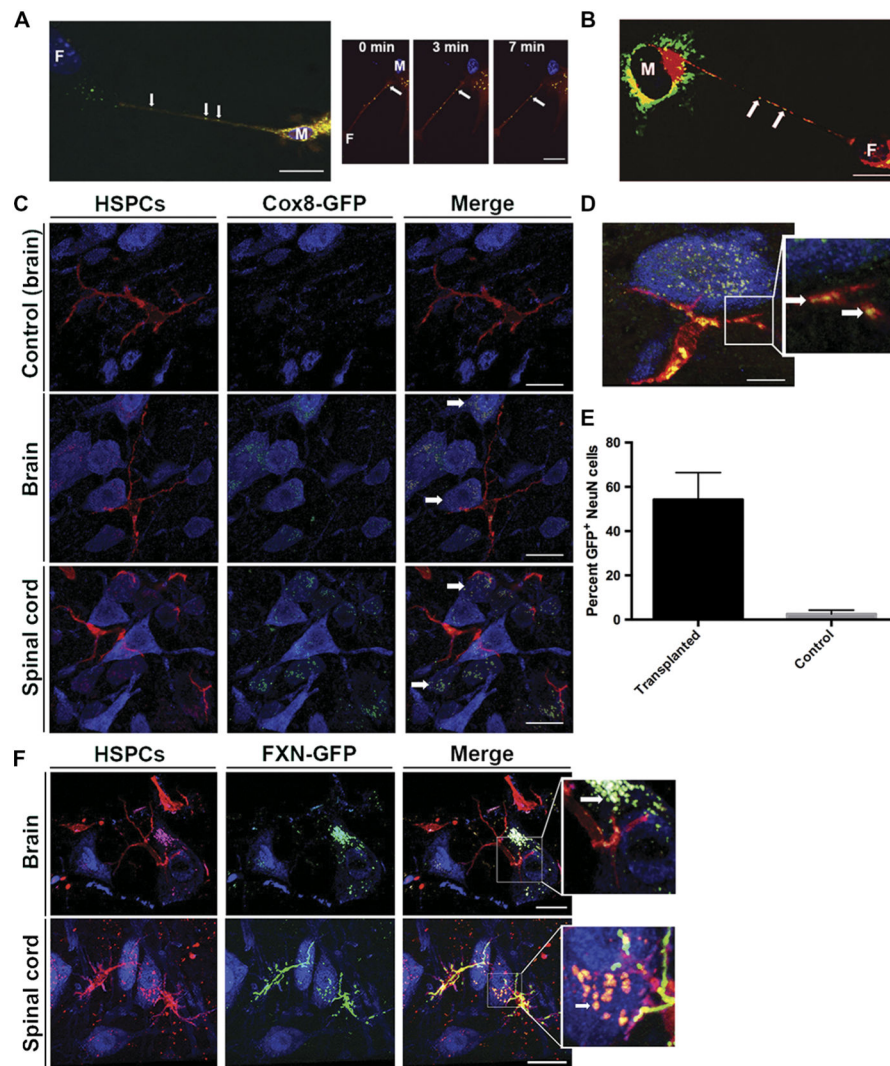
Fig. 4. Wild-type mouse HSPC-derived cells deliver frataxin and Cox8 to FRDA cells in vitro and in vivo

(**A** and **B**) Representative frames from confocal imaging movies of YG8R mouse fibroblasts (F) cocultured with (A) primary macrophages (M) isolated from a DsRed Cox8-GFP transgenic mouse (video S2) or (B) IC-21 macrophages transduced with LV-hFXN-GFP and stained with a MitoTracker Red (video S3). Scale bars, 10 μm. (**C**) Representative confocal images of brain sections from a YG8R mouse transplanted with DsRed[+] HSPCs (control; see video S4) and those of brain and spinal cord sections from a YG8R mouse transplanted with DsRed[+]/Cox8-GFP[+] HSPCs at 7 months after transplantation, labeled with an anti-NeuN antibody (blue) (see fig. S4 for the DRG, heart, and muscle). White arrows depict Cox8-GFP in recipient mouse neurons in the brain and spinal cord (see videos S5 and S6 for 3D visualization). Scale bars, 10 μm. (**D**) Representative confocal images of a spinal cord section from a YG8R mouse transplanted with DsRed[+]/Cox8-GFP[+] HSPCs at 7 months after transplantation, labeled with an anti-NeuN antibody (blue). White arrows depict Cox8-GFP within branch extensions of the DsRed[+] microglial cell. Scale bar, 5 μm. (**E**) Quantification of neurons containing Cox8-GFP in the cervical spinal cord gray matter of

YG8R mice transplanted with DsRed[+]/Cox8-GFP[+] HSPCs at 7 months after transplantation (see fig. S4 for the description of the automatic unbiased quantification method). (**F**) Representative confocal images of brain and spinal cord sections from a YG8R mouse transplanted with DsRed[+] HSPCs transduced with LV-hFXN-GFP at 7 months after transplantation and stained with anti-mCherry (red) and anti-NeuN (blue) antibodies. Scale bars, 10 μm.